iScience

CellPress
OPEN ACCESS

Article

Twinning-mediated anomalous alignment of rutile films revealed by synchrotron X-ray nanodiffraction

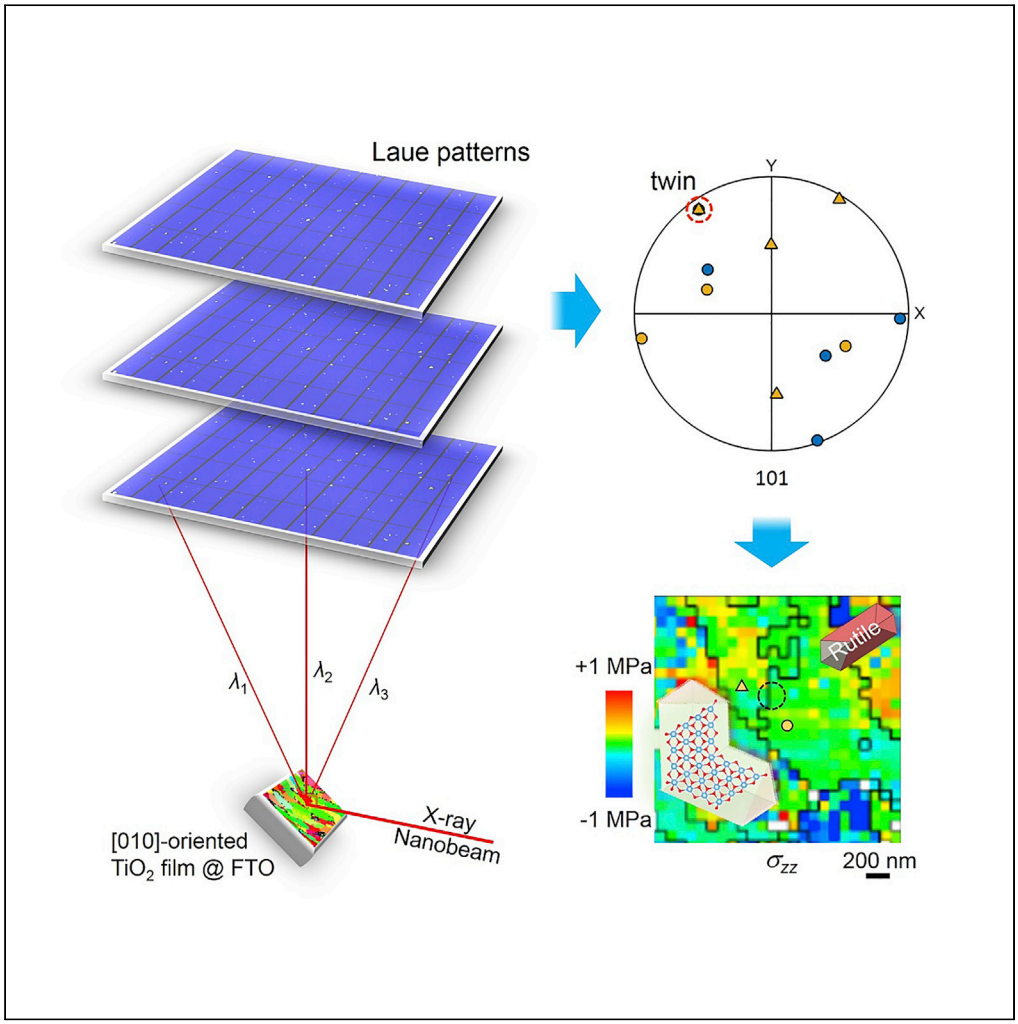

Yang Lu, Ching-Yu Chiang, Yao Li, ..., Eugene Huang, Bin Chen, Nobumichi Tamura

yang.lu@hpstar.ac.cn (Y.L.)
chiang.cy@nsrrc.org.tw (C.-Y.C.)
yanh@idsse.ac.cn (H.Y.)

Highlights

Nanotwinned TiO_2 film possesses stronger preferred orientation than its FTO substrate

State-of-the-art nanoscanned X-ray Laue diffraction is used to unveil the mechanism

Twinning-mediated heteroepitaxy mainly leads to the texture improvement

This work helps to stimulate the rational design and synthesis of nanotwin materials

Lu et al., iScience *24*, 102278
April 23, 2021
https://doi.org/10.1016/j.isci.2021.102278

iScience

CellPress
OPEN ACCESS

Article

Twinning-mediated anomalous alignment of rutile films revealed by synchrotron X-ray nanodiffraction

Yang Lu,[1,*] Ching-Yu Chiang,[2,*] Yao Li,[3] Ching-Shun Ku,[2] Hao Yan,[4,6,*] Eugene Huang,[1] Bin Chen,[1] and Nobumichi Tamura[5]

SUMMARY

Nanotwin structures in materials engender fascinating exotic properties. However, twinning usually alter the crystal orientation, resulting in random orientation and limited performances. Here, we report a well-aligned rutile TiO_2 nanotwin film with superior preferential orientation than its isostructural substrate. By means of the synchrotron X-ray Laue nanodiffraction technique, the crystal orientation, twin boundaries, and deviatoric stresses of the film were quantitatively imaged at unprecedented spatial resolution to unravel the underlying mechanism of this anomalous alignment. Massive {101}-type rutile nanotwins were observed, and a crystallographic relationship of the heteroepitaxy was proposed. The rapid twinning and twin-controlled heteroepitaxy are responsible for the texture improvement. This work would open up opportunities for rational design of better twin-based functional materials, and implies the powerful capabilities of X-ray nanodiffraction technique for multidisciplinary applications.

INTRODUCTION

Twinned crystals, especially the ordered and dense nanotwins, have attracted considerable interest due to their unique interface or defect structures, novel properties, and promising application prospects (Lu et al., 2009; Behrens et al., 2012; Nie et al., 2015; Zhu et al., 2018; Liu et al., 2018). Generally, a coherent twin boundary (TB) could be deemed as a stable two-dimensional (2D) high-pressure polymorph of the parent crystal due to its higher atomic density (e.g., rutile TiO_2 {101} twin (Hwang et al., 2000)). Similar to high-angle grain boundaries (GBs), TBs can serve as barriers against dislocation motion, that is, the hardening effect (Lu et al., 2009; Zhang et al., 2004). The excess energy of coherent TBs is about one order of magnitude lower than that of the ordinary high-angle GBs, which together with the hardening effect make twinned materials possess higher hardness, higher stability, higher toughness, lower compressibility, and near zero thermal expansion (Tian et al., 2013; Huang et al., 2014; Lu et al., 2004, 2009; Zhu et al., 2018; Zhang et al., 2004). In addition, the electrical conductivity of coherent TBs is higher than that of high-angle GBs, and the enhanced ionic transportation along TBs was observed in compounds such as WO_3 and SnO_2 (Lu et al., 2004; Aird and Salje, 2000; Nie et al., 2015). Moreover, the (photo)catalytic activity of a (photo)catalyst can be enhanced by nanotwin domains via twin-induced active sites or homojunctions caused by staggered band alignment (Behrens et al., 2012; Liu et al., 2011; Huang et al., 2018; Lu et al., 2020a, 2020b).

As an important class of multifunctional materials, rutile TiO_2 can be twinned on (101) and (301) planes (Hwang et al., 2000; Li et al., 1999; Lu et al., 2012a, 2020a; Jordan et al., 2018; Gao et al., 1992; Daneu et al., 2007, 2014). However, the synthetic TiO_2 twins generally possess lower texture because twinning trends to alter the growth direction or crystal orientation, which is detrimental to practical applications and the discovery of novel properties, whereas the natural rutile twin minerals can directionally form on their substrates (Li et al., 1999; Lu et al., 2012a; Jordan et al., 2018; Gao et al., 1991, 1992; Daneu et al., 2007, 2014; Lee et al., 2006; Sosnowchik et al., 2010). Recently, we have successfully synthesized rutile TiO_2 nanotwin films on fluorine-doped tin oxide (FTO) glass substrates with the rare *b*-axis preferred orientation (instead of the *c*-axis in common self-aligned rutile films) via a rapid nucleation/twinning strategy (Lu et al., 2020a). In this study, to uncover the underlying mechanism of the anomalous alignment, we applied the state-of-the-art scanning synchrotron X-ray Laue nanodiffraction technique (XND, see supplemental

[1]Center for High Pressure Science & Technology Advanced Research, Shanghai 201203, China

[2]National Synchrotron Radiation Research Center, Hsinchu 30076, Taiwan

[3]School of Materials Science and Engineering, Chang'an University, Xi'an, Shaanxi 710064, China

[4]CAS Key Laboratory of Experimental Study under Deep-sea Extreme Conditions, Institute of Deep-Sea Science and Engineering, Chinese Academy of Sciences, Sanya 572000, China

[5]Advanced Light Source, Lawrence Berkeley National Laboratory, Berkeley, CA 94720, USA

[6]Lead contact

*Correspondence: yang.lu@hpstar.ac.cn (Y.L.), chiang.cy@nsrrc.org.tw (C.-Y.C.), yanh@idsse.ac.cn (H.Y.)

https://doi.org/10.1016/j.isci.2021.102278

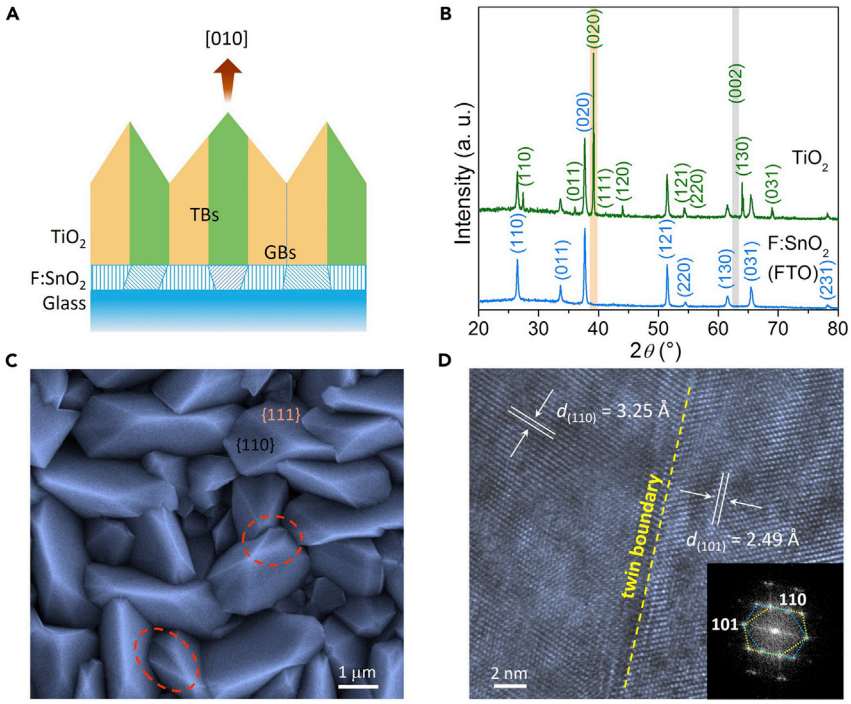

Figure 1. Texture-improved rutile TiO_2 twin film on F-doped SnO_2 substrate

(A) Schematic illustration of the rutile TiO_2 twin film on FTO (or F:SnO_2) substrate (side view).

(B) XRD patterns of the rutile TiO_2 twin film and the FTO conductive glass substrate.

(C) SEM image of the rutile TiO_2 twin crystals. The red dashed circles indicate the reentrant facets.

(D) TEM image of the twinned TiO_2. Inset is the corresponding fast Fourier transformation (FFT) pattern.

information Figure S1) and the developed data analyzing software to image the crystal orientation, twin boundaries, and stresses at ~80 nm spatial resolution. A rutile {101} twin model on the substrate was proposed to illustrate the anomalous orientation. This study will facilitate the rational design and fabrication of better nanostructured materials.

RESULTS AND DISCUSSION

Characterization of [010]-oriented rutile twin films

Several methods can be adopted to determine the crystal orientation and grain boundaries in materials, including electron backscatter diffraction (EBSD), transmission electron microscopy (TEM), and electron tomography (Hsiao et al., 2012; Schwartz et al., 2009; Langille et al., 2012; Fultz and Howe, 2008; Midgley and Dunin-Borkowski, 2009). Although EBSD can image the orientation and twin boundaries of the crystals on the surface, the surface of the sample is required to be flat and the angular resolution is limited to 1–0.1° (Schwartz et al., 2009; Hsiao et al., 2012). TEM and electron tomography can characterize the crystal structure and twin boundaries or flat interfaces in an atomic resolution (Fultz and Howe, 2008; Midgley and Dunin-Borkowski, 2009; Langille et al., 2012), but the specimen preparation is complicated or the sample should be small/thin (generally, size/thickness <100 nm) due to the low penetration depth of electron beam. X-ray diffraction (XRD) in laboratory provides the ensemble-average crystal structure of multiple grains (size >1 μm). Alternatively, the high-brilliance X-ray nanobeam with strong penetration capacity enables the quantitative and nondestructive mapping of crystal orientation and buried grain boundaries of bulk/thick sample with larger strain and surface roughness by X-ray nanodiffraction (Chen et al., 2016), which makes it suitable for studying nanotwinned materials and *in situ* probing the processes of the growth and transformation of materials at extreme conditions, e.g., high/low temperature and high pressure/stress.

The TiO_2 films (Figure 1A) were synthesized on the FTO glass substrates by a rapid reaction method (see transparent methods) (Lu et al., 2020a). The XRD patterns (Figures 1B and S2) show that the TiO_2 film and

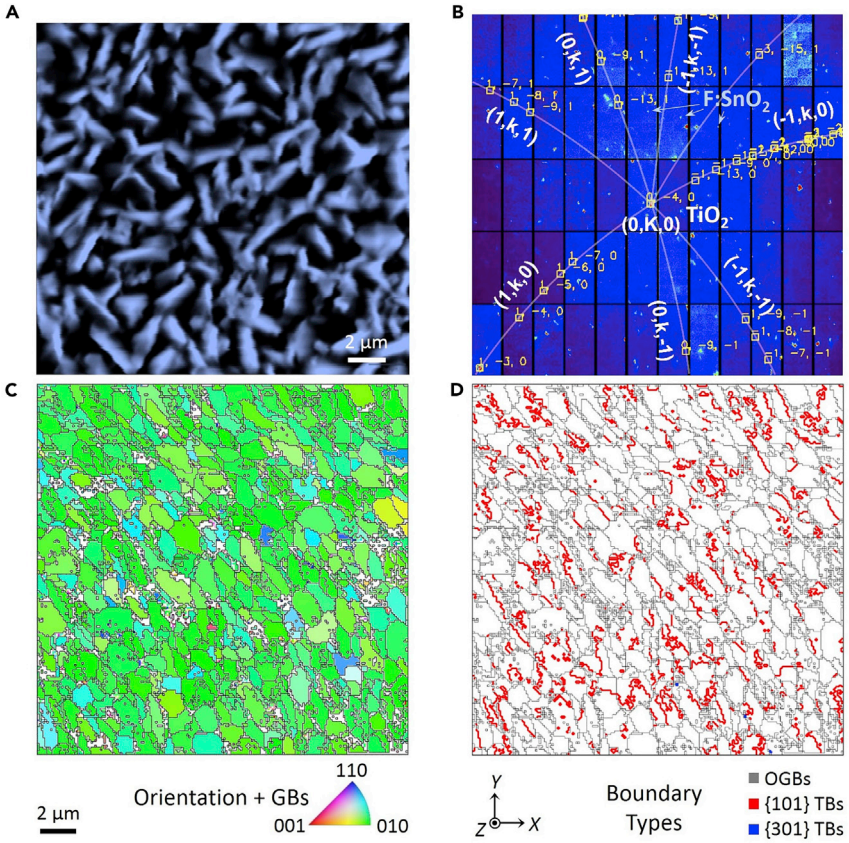

Figure 2. Nanoimaging of morphology, crystal orientation, and twin boundaries of rutile film

(A) SEM image of the TiO_2 film around the scanning region (~20 μm × 20 μm).

(B) Typical indexed XND image of the film (No. 14993).

(C) Crystal orientation map for TiO_2 grains along the normal direction of film (*z* axis) overlapped with grain boundaries (GBs). The white or transparent area represents the patterns failed to be indexed as rutile structure due to the complex or weak diffraction patterns from the joint area of grains.

(D) Spatial distribution of ordinary grain boundaries (OGBs, gray), {101} twin boundaries (red), and {301} twin boundaries (blue). Scale bar (bottom left) for Figures 2C and 2D: 2 μm. Sample coordinate system (bottom) for Figures 2C and 2D: *O-XYZ*.

FTO substrate are of rutile structure and a preferred orientation of TiO_2 film along the [010] direction, with a degree about 16 times stronger than that of the isostructural substrate. The scanning electron mircroscopy (SEM) image (Figure 1C) shows the ship-like rutile TiO_2 crystals inverted on the substrate, with predominant exposed {111} and {110} facets (Lu et al., 2020a). Notably, there is a handful of crystals with reentrant shape, symbolizing twinned crystals. The high-resolution TEM image (Figure 1D) demonstrates that the sample possesses twin structure with a composition plane of (101). The thickness of the rutile twin film is about 2 μm (Figure S3).

Laue nanoimaging of crystal orientation and twin boundaries

The dedicated XND setup of Taiwan Photon Source (TPS, beamline 21A) (Figure S1) can achieve an angular resolution down to 0.01°, with a nanoscale spatial resolution (~80 nm in this work), and the deviatoric strain tensors resolution of 10^{-4} (Chung and Ice, 1999). Figure 2A shows the SEM image of the rutile twin film surrounding the XND-scanned region. A representative XND image (No. 14993) of the film was indexed as rutile phase (see Figure 2B). The (0, K, 0) spot of TiO_2 located near the center of the Laue image indicates that the *a*- or *b*-axis preferred orientation of the grain as inferred from the geometric relationship of the X-ray, sample, and detector (Figure S1). In the scanned region, there are 40,401 images recorded and auto-indexed. As shown in Figure 2C, the crystal orientation map (overlapped with grain boundaries) of the film along the normal direction (*z* axis, other directions can be find in Figures S4A and S4B) is predominantly

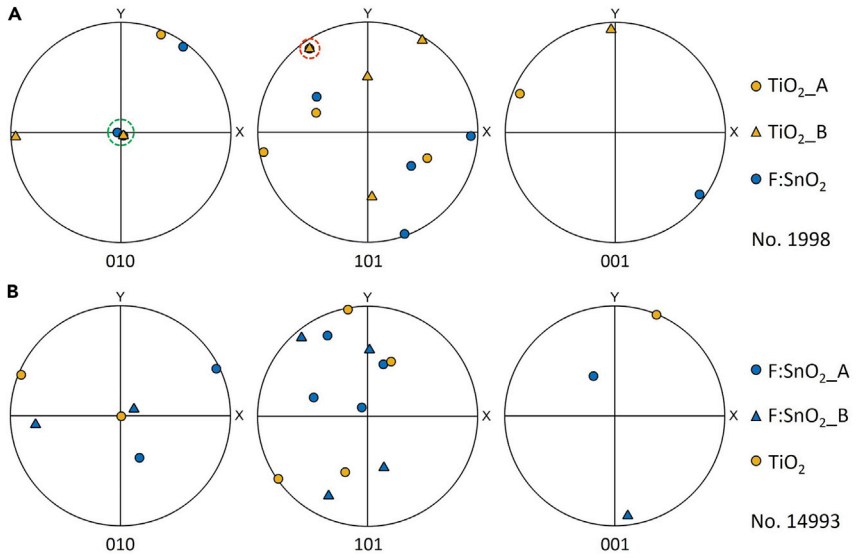

Figure 3. Pole figures derived from typical XND images

(A) XND image of No. 1998.

(B) XND image of No. 14993.

occupied by green area with only little blue and red area, revealing that the TiO_2 film is preferentially oriented with the (100) or (010) crystal planes parallel to the glass substrate.

Previous studies showed that in the synthetic rutile phase TiO_2 powder or natural rutile minerals, the {101} and {301} twins are usually present together, with around six times many former than the latter (Li et al., 1999; Lu et al., 2012a; Jordan et al., 2018; Gao et al., 1992; Daneu et al., 2007, 2014). In our case, the possible twin boundaries were identified from the ordinary grain boundaries by checking the rotation angle of adjacent gains and the parallelity of their rotation axis (Li et al., 2015). As shown in Figure 2D, the red dots or lines signify that the grain boundaries fit well with the {101} twin boundaries, judging from the fact that the rotation angle of the adjacent grains along the [010] axis is 114.4° for the rutile {101}/[010] twin. The blue dots represent that the GBs match well with the {301} TBs (the mutual rotation angle of the rutile {301}/[010] twin is 54.7° (Lee et al., 1993)). Obviously, massive {101}-type rutile twins were detected, whereas only a few blue dots are observed in the map, which suggests the ratio and weight of the rutile {301} twins in the film are much lower than that reported elsewhere. We note that there are lots of nanotwins with thickness less than 80 nm in the film, which have been demonstrated by TEM observation (Lu et al., 2020a).

Taking the XND image of No. 1998 as an example, the image can be indexed as two sets of Laue diffraction spots of rutile TiO_2 and one set of Laue diffraction spots of F-doped SnO_2 (Figure S5 and Data S1). The orientation of both crystals plotted as pole figures shown in Figure 3A reveal that two {010} poles and two {101} poles overlap, respectively, i.e., {101} as composition planes and [010] as a twin axis. The misorientation between both twinned components is 65.66°/[0.0025 1.0000 0.0005], agreeing well with the theoretical 65.57°/[0 1 0]. Moreover, the XND image of No. 14993 was indexed as one set of Laue diffraction spots of rutile TiO_2 and two sets of Laue diffraction spots of F-doped SnO_2 (Figures 2B and S6). The corresponding pole figures (Figure 3B) indicate that the preferential [010] orientation of F:SnO_2 substrate is weaker than that of TiO_2 overlayer, which is consistent with the XRD spectra, crystal orientation maps, and pole figures (Figures 1B, S4, and S7).

Formation mechanism of well-aligned nanotwin film

During the process of rapid hydrothermal synthesis of our samples, there are roughly three mechanisms at play: (1) nucleation of twins in reactive solution, (2) attachment of twinned crystals or nuclei to the substrate, and (3) selective growth controlled by twin anisotropy. In growth twin, twinning is usually related to the stress partially generated by the presence of defects and impurities or the accidental attachment of crystalline grains during the initial stages of crystal growth (Penn and Banfield, 1998, 1999; Lebensohn and

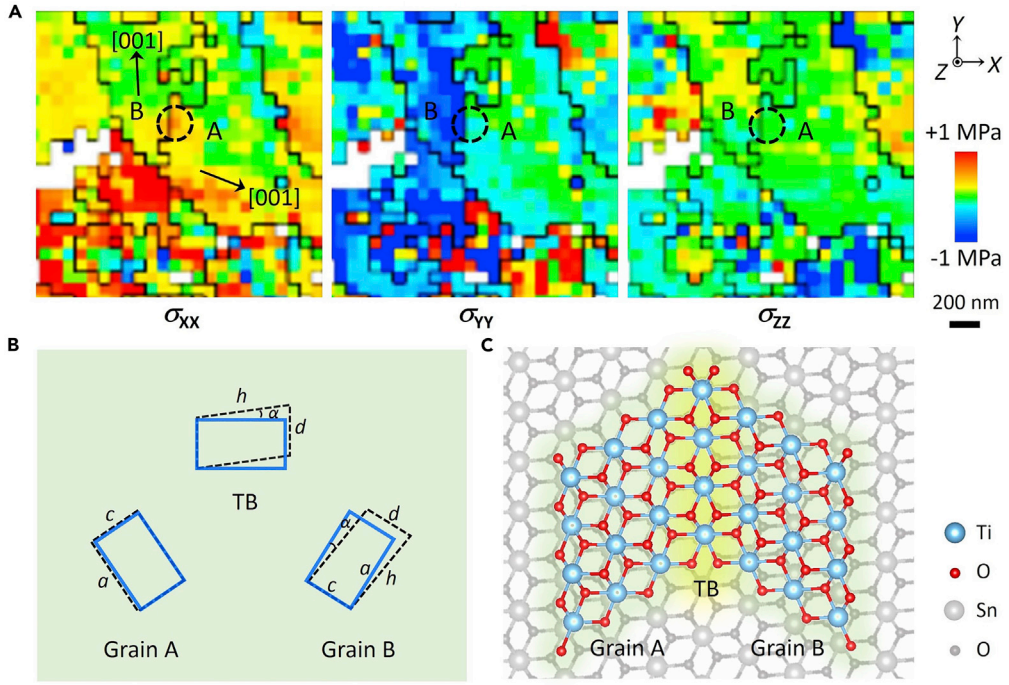

Figure 4. Strain distribution and twin-substrate model

(A) Spatial distributions of the normalized deviatoric stresses in the typical twinned rutile grains. The position of No. 1998 is denoted by dashed circles.

(B) Lattice mismatch between rutile TiO_2 (blue line) and F:SnO_2 (black dashed line). The angular mismatch (α) is around 7.5°.

(C) Scheme of the [010]-oriented rutile TiO_2 {101} twin on the SnO_2(010) viewed along the [010] direction.

Tomé, 1993; Guermazi et al., 1985; Bursill et al., 1969). To reveal the mechanisms of twinning and attachment, crystallographic relationships and the stress distribution in the rutile nanotwin film were further analyzed. As shown in Figures 4A and S8, the uneven distribution of deviatoric stresses in rutile twin film suggests that the formation or attachment of twinned rutile crystals on the substrate is associated with the stress. In addition, twinned particles were discovered in the reaction solution, and their shape is related to that of twins grown on the substrate (Figure S9) (Lu et al., 2020a). During the dynamic dissolution of reaction precursor (TiN) at room temperature or rapidly elevated temperature, the generation of oxygen vacancies (Ti^{3+}, see the electron paramagnetic resonance data in our previous work (Lu et al., 2020a)) or N species would induce twin nuclei to reduce the system energy at the initial reaction stage. Then, the rutile twin seeds attach and continuously grow on the F:SnO_2 substrate. Hence, the F:SnO_2 substrate is not the prerequisite for twinning but profoundly impact the heteroepitaxial growth and the preferred orientation of the TiO_2 overlayer.

An atomic model of rutile {101} twin on SnO_2 was proposed, as shown in Figure 4C, based on the pole figures such as No. 1998, strain distributions, and previous studies (Lu et al., 2012b; Lee et al., 1993). Table 1 and Figure 4B show the lattice mismatch between rutile twin and substrate. It was found that the lattice mismatch between the isostructural F:SnO_2 and one twin component (Grain A and twin boundary) is lower than 8%, which could facilitate its heteroepitaxy on F:SnO_2 grains and the formation of the other twin component (Grain B) with [010]-preferred orientation regardless of the large (tensile or compressive) stress in the Grain B region (Steidl et al., 2017). Similar effect can be obtained in the case of the rutile {301} twin formation (Figure S10). Rutile twin can be grown on some types of hexagonal substrates, such as sapphire (Al_2O_3) (Gao et al., 1992; Lee et al., 2006) and hematite (α-Fe_2O_3) (Rečnik et al., 2015) or formed from other hexagonal precursors, e.g., ilmenite ($FeTiO_3$) (Janssen et al., 2010; Stanković et al., 2015; Daneu et al., 2014). Interestingly, the (010)-oriented SnO_2 substrate possesses an approximatively hexagonal atomic arrangement, showing the importance of the lattice-matching attachment in the twinning and heteroepitaxial growth. The attachment of twinned rutile nanocrystals onto SnO_2 substrate may be controlled by some

Table 1. Lattice mismatch between the rutile TiO_2 {101} twin and F:SnO_2 substrate

	Grain A region		Twin boundary		Grain B region	
	a (Å)	*c* (Å)	*d* (Å)	*h* (Å)	*a* or *h* (Å)	*c* or *d* (Å)
TiO_2	4.5940	2.9590	2.7322	4.9753	4.5940	2.9590
F:SnO_2	4.7687	3.2036	2.8724	5.3644	5.3644	2.8724
Mismatch	3.73%	7.94%	5.00%	7.53%	15.47%	−2.97%

mode of van der Waals-force-driven self-assembly processes, as described in references (Penn and Banfield, 1998; Jordan et al., 2018). In this case, the orientation relationship between SnO_2 and TiO_2 is expected to be imperfect, as shown by XND data (Figure S4).

In previous studies, the untwinned rutile TiO_2 films of nanorods or nanowires that were grown on FTO substrates commonly possess the [001]-preferred orientation, although the preferential orientation of FTO substrates is [010] direction (Lu et al., 2019; Liu and Aydil, 2009; Feng et al., 2008). The erected growth of untwinned prismatic rutile on substrates could suppress the prostrate growth due to the fact that the fastest growth rate is along [001] direction, which can account for the self-aligned behavior of one-dimensional rutile arrays on [010]-oriented substrates. From the view point of surface free energy, the tips of rutile nanorods or nanowires are commonly exposed with reactive high-energy facets ({111}, {001}, or {101}), which favors the fastest growth along [001] direction and the formation of lateral low-energy {110} facets (Lu et al., 2019, 2020a). However, in our case, after twinned TiO_2 is formed, the [001] direction ceases to be the fastest growth direction. Instead, the twin plane becomes the fastest growth direction, pulling the rest of rutile crystal along its way. This is supported by the fact that the ship-like rutile twins mainly are predominated with {111} facets (some capping species may be formed in the rapid reaction environments). In effect, this type of geometric control actually governs crystal orientation in the TiO_2 film, whereas the substrate only plays a minor role. Any crystals that have unfavorable orientations (with twin plane not vertical to the substrate) will be blocked by surrounding seeds, and only those that have twin plane oriented vertically to the substrate can grow freely. It is likely that they would grow in a similar manner on any substrate other than FTO, as described for ZnO films by Podlogar et al. (Podlogar et al., 2012). Therefore, the discovered texture improvement could be ascribed to the rapid formation of twinned seeds on the preferred orientation of FTO substrate in the special reaction environments.

CONCLUSIONS

In conclusion, the twin law and crystallographic texture in the anomalously aligned TiO_2 nanotwin film were systematically analyzed by the synchrotron X-ray Laue nanodiffraction. The anomalous alignment was mainly ascribed to the twin-mediated heteroepitaxy with low lattice mismatch. This study also presents a state-of-the-art tool to investigate the twin structure, crystal orientation, and internal strain of functional materials at sub-100 nm resolution and would stimulate the widespread application of X-ray Laue nanodiffraction in materials science, geoscience, solar cells, and electronic and optoelectronic devices. With the rapid developments of X-ray focusing optics and advanced synchrotron light sources, we expect that the X-ray Laue nanodiffraction system will further enable the quantitative 2D/3D imaging of materials at several nanometers resolution.

Limitations of the study

It is not clear whether rutile {301} twins are present or not in the film. The orientation maps of FTO may be distorted because the grain size is too small and the software (XMAS, 2018) cannot automatically remove the indexed points from TiO_2 during the auto-indexing.

Resource availability

Lead contact

yanh@idsse.ac.cn.

Lead contact

yang.lu@hpstar.ac.cn.

Data and code availability

yang.lu@hpstar.ac.cn; chiang.cy@nsrrc.org.tw.

METHODS

All methods can be found in the accompanying transparent methods supplemental file .

SUPPLEMENTAL INFORMATION

Supplemental information can be found online at https://doi.org/10.1016/j.isci.2021.102278.

ACKNOWLEDGMENTS

This work was partially supported by the National Science Associated Funding (NSAF, Grant No. U1530402) and the National Natural Science Foundation of China (NSFC, Grant No. 42050203). We gratefully acknowledge Drs. C. H. Lin and S. J. Chiu at TPS for experimental assistance. We thank Ms. Y. P. Yang of HPSTAR for the fabrication of TEM specimen and Ms. F. O'Toole of HPSTAR for polishing of the manuscript.

AUTHOR CONTRIBUTIONS

Conceptualization, Y.Lu and H.Y.; Methodology, Y.Lu, C.S.K., C.Y.C., Y.Li, and H.Y.; Investigation, C.Y.C., Y.Li, Y.Lu, and N.T.; Writing—Original Draft, Y.Lu; Writing—Review and Editing, Y.Lu, E.H., H.Y., and B.C.

DECLARATION OF INTERESTS

The authors declare no competing interests.

Received: January 24, 2021
Revised: February 23, 2021
Accepted: March 2, 2021
Published: April 23, 2021

REFERENCES

Aird, A., and Salje, E.K.H. (2000). Enhanced reactivity of domain walls in WO_3 with sodium. Eur. Phys. J. B *15*, 205–210.

Behrens, M., Studt, F., Kasatkin, I., Kuhl, S., Havecker, M., Abild-Pedersen, F., Zander, S., Girgsdies, F., Kurr, P., Kniep, B.L., et al. (2012). The active site of methanol synthesis over Cu/ZnO/Al_2O_3 industrial catalysts. Science *336*, 893–897.

Bursill, L.A., Hyde, B.G., Terasaki, O., and Watanabe, D. (1969). On a new family of titanium oxides and the nature of slightly-reduced rutile. Philos. Mag. *20*, 347–359.

Chen, X., Dejoie, C., Jiang, T., Ku, C.-S., and Tamura, N. (2016). Quantitative microstructural imaging by scanning Laue x-ray micro- and nanodiffraction. MRS Bull *41*, 445–453.

Chung, J.-S., and Ice, G.E. (1999). Automated indexing for texture and strain measurement with broad-bandpass x-ray microbeams. J. Appl. Phys. *86*, 5249–5255.

Daneu, N., Rečnik, A., and Mader, W. (2014). Atomic structure and formation mechanism of (101) rutile twins from Diamantina (Brazil). Am. Mineral. *99*, 612–624.

Daneu, N., Schmid, H., Recnik, A., and Mader, W. (2007). Atomic structure and formation mechanism of (301) rutile twins from Diamantina (Brazil). Am. Miner. *92*, 1789–1799.

Feng, X.J., Shankar, K., Varghese, O.K., Paulose, M., Latempa, T.J., and Grimes, C.A. (2008). Vertically aligned single crystal TiO_2 nanowire arrays grown directly on transparent conducting oxide coated glass: synthesis details and applications. Nano Lett. *8*, 3781–3786.

Fultz, B., and Howe, J.M. (2008). Transmission Electron Microscopy and Diffractometry of Materials (Springer).

Gao, Y., Merkle, K.L., Chang, H.L., Zhang, T.J., and Lam, D.J. (1992). Study of defects and interfaces on the atomic scale in epitaxial TiO_2 thin films on sapphire. Philos. Mag. A. *65*, 1103–1125.

Gao, Y., Merkle, K.L., Chang, H.L.M., and Lam, T.J.Z.D.J. (1991). Microstructure of TiO_2 rutile thin films deposited on (110) $\alpha-Al_2O_3$. J. Mater. Res. *6*, 2417–2426.

Guermazi, M., Thevenard, P., and Blanchin, M.G. (1985). Chemical twinning induced by chemical implantation in TiO_2. Radiat. Eff. *91*, 125–137.

Hsiao, H.Y., Liu, C.M., Lin, H.W., Liu, T.C., Lu, C.L., Huang, Y.S., Chen, C., and Tu, K.N. (2012). Unidirectional growth of microbumps on (111)-oriented and nanotwinned copper. Science *336*, 1007–1010.

Huang, M., Li, C., Zhang, L., Chen, Q., Zhen, Z., Li, Z., and Zhu, H. (2018). Twin structure in $BiVO_4$ photoanodes boosting water oxidation performance through enhanced charge separation and transport. Adv. Energy Mater. *8*, 1802198.

Huang, Q., Yu, D., Xu, B., Hu, W., Ma, Y., Wang, Y., Zhao, Z., Wen, B., He, J., Liu, Z., and Tian, Y. (2014). Nanotwinned diamond with unprecedented hardness and stability. Nature *510*, 250–253.

Hwang, S.-L., Shen, P., Chu, H.-T., and Yui, T.-F. (2000). Nanometer-size α-PbO_2-type TiO_2 in garnet: a thermobarometer for ultrahigh-pressure metamorphism. Science *288*, 321–324.

Janssen, A., Putnis, A., Geisler, T., and Putnis, C.V. (2010). The experimental replacement of ilmenite by rutile in HCl solutions. Mineral. Mag. *74*, 633–644.

Jordan, V., Dasireddy, V.D.B.C., Likozar, B., Podgornik, A., and Rečnik, A. (2018). Material's design beyond lateral attachment: twin-controlled spatial branching of rutile TiO_2. Cryst. Growth Des. *18*, 4484–4494.

Langille, M.R., Zhang, J., Personick, M.L., Li, S., and Mirkin, C.A. (2012). Stepwise evolution of spherical seeds into 20-fold twinned icosahedra. Science *337*, 954–957.

Lebensohn, R.A., and Tomé, C.N. (1993). A study of the stress state associated with twin nucleation and propagation in anisotropic materials. Philos. Mag. A. *67*, 187–206.

Lee, J.-C., Park, K.-S., Kim, T.-G., Choi, H.-J., and Sung, Y.-M. (2006). Controlled growth of high-quality TiO_2 nanowires on sapphire and silica. Nanotechnology *17*, 4317–4321.

Lee, W.Y., Bristowe, P.D., Gao, Y., and Merkle, K.L. (1993). The atomic structure of twin boundaries in rutile. Philos. Mag. Lett. *68*, 309–314.

Li, G.L., Wang, G.H., and Hong, J.M. (1999). Morphologies of rutile form TiO_2 twins crystals. J. Mater. Sci. Lett. *18*, 1243–1246.

Li, Y., Wan, L., and Chen, K. (2015). A look-up table based approach to characterize crystal twinning for synchrotron X-ray Laue microdiffraction scans. J. Appl. Crystallogr. *48*, 747–757.

Liu, B., and Aydil, E.S. (2009). Growth of oriented single-crystalline rutile TiO_2 nanorods on transparent conducting substrates for dye-sensitized solar cells. J. Am. Chem. Soc. *131*, 3985–3990.

Liu, M., Wang, L., Lu, G., Yao, X., and Guo, L. (2011). Twins in $Cd_{1-x}Zn_xS$ solid solution: highly efficient photocatalyst for hydrogen generation from water. Energy Environ. Sci. *4*, 1372–1378.

Liu, Y., Collins, L., Proksch, R., Kim, S., Watson, B.R., Doughty, B., Calhoun, T.R., Ahmadi, M., Ievlev, A.V., Jesse, S., et al. (2018). Chemical nature of ferroelastic twin domains in $CH_3NH_3PbI_3$ perovskite. Nat. Mater. *17*, 1013–1019.

Lu, K., Lu, L., and Suresh, S. (2009). Strengthening materials by engineering coherent internal boundaries at the nanoscale. Science *324*, 349–352.

Lu, L., Shen, Y.F., Chen, X.H., Qian, L.H., and Lu, K. (2004). Ultrahigh strength and high electrical conductivity in copper. Science *304*, 422–426.

Lu, W., Bruner, B., Casillas, G., He, J., Jose-Yacaman, M., and Farmer, P.J. (2012a). Large scale synthesis of V-shaped rutile twinned nanorods. CrystEngComm *14*, 3120–3124.

Lu, W., Bruner, B., Casillas, G., Mejia-Rosales, S., Farmer, P.J., and Jose-Yacaman, M. (2012b). Direct oxygen imaging in titania nanocrystals. Nanotechnology *23*, 335706.

Lu, Y., Chiang, C.-Y., and Huang, E. (2020a). Vertically nanotwinned TiO_2 photoanodes with enhanced charge transport for efficient solar water splitting. Appl. Mater. Today *20*, 100707.

Lu, Y., Liu, X., Liu, H., Wang, Y., Liu, P., Zhu, X., Zhang, Y., Zhang, H., Wang, G., Lin, Y., et al. (2020b). Selective growth of high density anatase {101} twin boundaries on high energy {001} facets. Small Struct. 2000025.

Lu, Y., Wei, Z., Salke, P.N., Yu, L., and Yan, H. (2019). Enhanced electron transport in rutile TiO_2 nanowires via H_2S-assisted incorporation of dissolved silicon for solar-driven water splitting. Appl. Catal. B Environ. *244*, 767–772.

Midgley, P.A., and Dunin-Borkowski, R.E. (2009). Electron tomography and holography in materials science. Nat. Mater. *8*, 271–280.

Nie, A.M., Gan, L.Y., Cheng, Y.C., Li, Q.Q., Yuan, Y.F., Mashayek, F., Wang, H.T., Klie, R., Schwingenschlogl, U., and Shahbazian-Yassar, R. (2015). Twin boundary-assisted lithium ion transport. Nano Lett. *15*, 610–615.

Penn, R.L., and Banfield, J.F. (1998). Oriented attachment and growth, twinning, polytypism, and formation of metastable phases: insights from nanocrystalline TiO_2. Am. Mineral. *83*, 1077–1082.

Penn, R.L., and Banfield, J.F. (1999). Formation of rutile nuclei at anatase {112} twin interfaces and the phase transformation mechanism in nanocrystalline titania. Am. Mineral. *84*, 871–876.

Podlogar, M., Richardson, J.J., Vengust, D., Daneu, N., Samardžija, Z., Bernik, S., and Rečnik, A. (2012). Growth of transparent and conductive polycrystalline (0001)-ZnO films on glass substrates under low-temperature hydrothermal conditions. Adv. Funct. Mater. *22*, 3136–3145.

Rečnik, A., Stanković, N., and Daneu, N. (2015). Topotaxial reactions during the genesis of oriented rutile/hematite intergrowths from Mwinilunga (Zambia). Contrib. Mineral. Petr. *169*, 19.

Schwartz, A.J., Kumar, M., Adams, B.L., and Field, D.P. (2009). Electron Backscatter Diffraction in Materials Science (Springer).

Sosnowchik, B.D., Chiamori, H.C., Ding, Y., Ha, J.-Y., Wang, Z.L., and Lin, L. (2010). Titanium dioxide nanoswords with highly reactive, photocatalytic facets. Nanotechnology *21*, 485601–485606.

Stanković, N., Rečnik, A., and Daneu, N. (2015). Topotaxial reactions during oxidation of ilmenite single crystal. J. Mater. Sci. *51*, 958–968.

Steidl, M., Koppka, C., Winterfeld, L., Peh, K., Galiana, B., Supplie, O., Kleinschmidt, P., Runge, E., and Hannappel, T. (2017). Impact of rotational twin boundaries and lattice mismatch on III-V nanowire growth. ACS Nano *11*, 8679–8689.

Tian, Y.J., Xu, B., Yu, D.L., Ma, Y.M., Wang, Y.B., Jiang, Y.B., Hu, W.T., Tang, C.C., Gao, Y.F., Luo, K., et al. (2013). Ultrahard nanotwinned cubic boron nitride. Nature *493*, 385–388.

Zhang, X., Misra, A., Wang, H., Shen, T.D., Nastasi, M., Mitchell, T.E., Hirth, J.P., Hoagland, R.G., and Embury, J.D. (2004). Enhanced hardening in Cu/330 stainless steel multilayers by nanoscale twinning. Acta Mater. *52*, 995–1002.

Zhu, H., Li, Q., Yang, C., Zhang, Q., Ren, Y., Gao, Q., Wang, N., Lin, K., Deng, J., Chen, J., et al. (2018). Twin crystal induced near zero thermal expansion in SnO_2 nanowires. J. Am. Chem. Soc. *140*, 7403–7406.

iScience, Volume *24*

Supplemental information

Twinning-mediated anomalous alignment of rutile films revealed by synchrotron X-ray nanodiffraction

Yang Lu, Ching-Yu Chiang, Yao Li, Ching-Shun Ku, Hao Yan, Eugene Huang, Bin Chen, and Nobumichi Tamura

Supplemental Information

Transparent Methods, Figures S1-S10, and Data S1

Transparent Methods

Synthesis

The well-aligned rutile TiO_2 twins were grown on fluorine-doped tin oxide (FTO) glass substrates by a rapid hydrothermal method (Lu et al., 2020). In a typical synthetic procedure, titanium nitride powder (40 mg, 99.5 wt%, size: 2-10 μm, aladdin), hydrochloric acid (26 mL, 5.0 M), and hydrogen peroxide (4 mL, 30 wt%) were placed in a Teflon-lined autoclave (100 mL in volume), in which two pieces of cleaned FTO conducting substrates were slantwise immersed with the conductive side facing down, then, heated quickly at 200 °C for 20 h in an electric oven (preheated to ~200 °C). After the hydrothermal procedure, the autoclave was took out and cooled naturally to room temperature. The obtained samples were washed with deionized water and dried in ambient environment.

Characterization

The crystal structure and preferential orientation of samples were investigated by the powder X-ray diffraction (XRD) on the X-ray diffractometer with Cu-Kα radiation (PANalytical X' Pert Pro, $\lambda_{k\alpha 1}$ = 1.540598 Å). The degree of the preferential orientation (p) of a film was estimated by the ratio (R) of peak intensity (e.g. $I_{(020)}$ / $I_{(110)}$) as compared with the ratio (R^0) of the reference powder without preferred orientation. That is, $p = R / R^0 = I_{(020)} / I_{(110)} / R^0$. We used JCPDS no. 96-900-4142 as the rutile reference (R^0 = 0.071), and JCPDS no. 01-077-0452 as the F:SnO_2 reference (R^0 = 0.207). The morphology and twin structure of samples were characterized by a field-emission scanning electron microscope (SEM, Hitachi SU8020) and a transmission electron microscope (TEM, FEI TECNAI G^2 S-TWIN). The cross-sectional TEM specimen (thinned TiO_2 ~ 80 nm) was prepared by a focused ion beam (FIB) and scanning electron microscope dual beam system (FEI Versa 3D).

X-ray Laue nanodiffraction experiments and data analysis

The synchrotron X-ray Laue nanodiffraction of film was conducted at the beamline BL21A of Taiwan Photon Source (TPS), where the FOcus x-Ray for Micro-Structure Analysis (FORMOSA) end-station provides an all-in-one solution including a large area hybrid pixel array detector (DECTRIS Pilatus3S 6M) on the top of the sample chamber and a built-in SEM (ORSAY PHYSICS) as an online real-time navigator (Chen et al., 2016). The TiO_2 film (on a holder) was mounted on an integrated hexapod scanner enabling the scanning measurements, and tilted 45° relative to the incident X-ray nanobeam. A series of scanning 2D polychromatic Laue diffraction patterns of sample were collected with an exposure time of 400 ms and the spatial resolution of ~80 nm at room temperature (Sample-CCD distance: 523.220 mm; Energy:

5-28 keV).

The crystal orientation and stress information were simultaneously determined from these patterns by the X-ray Microdiffraction Analysis Software (XMAS, Tamura, 2018) on personal computer and super-computer (Dell R220 computer clusters with 48 nodes, NSSRC). To map the crystal orientation, grain boundaries, and deviatoric stresses, the software automatically picked up the Laue pattern with the strongest intensity and indexed at least 6 reflections (or backscattering Laue points), i.e., only analyzed one TiO_2 grain per XND image. The twin law were determined by the self-developed software. The errors of both rotation angle and rotation axis of adjacent gains are less than 3° during the mapping of twin boundaries (Li et al., 2015). The used elastic stiffness tensor of rutile TiO_2 is

$$M = \begin{bmatrix} 2.6700 & 1.6500 & 1.5200 & 0 & 0 & 0 \\ 1.6500 & 2.6700 & 1.5200 & 0 & 0 & 0 \\ 1.5200 & 1.5200 & 4.8300 & 0 & 0 & 0 \\ 0 & 0 & 0 & 1.2200 & 0 & 0 \\ 0 & 0 & 0 & 0 & 1.2200 & 0 \\ 0 & 0 & 0 & 0 & 0 & 2.1200 \end{bmatrix}. \quad (1)$$

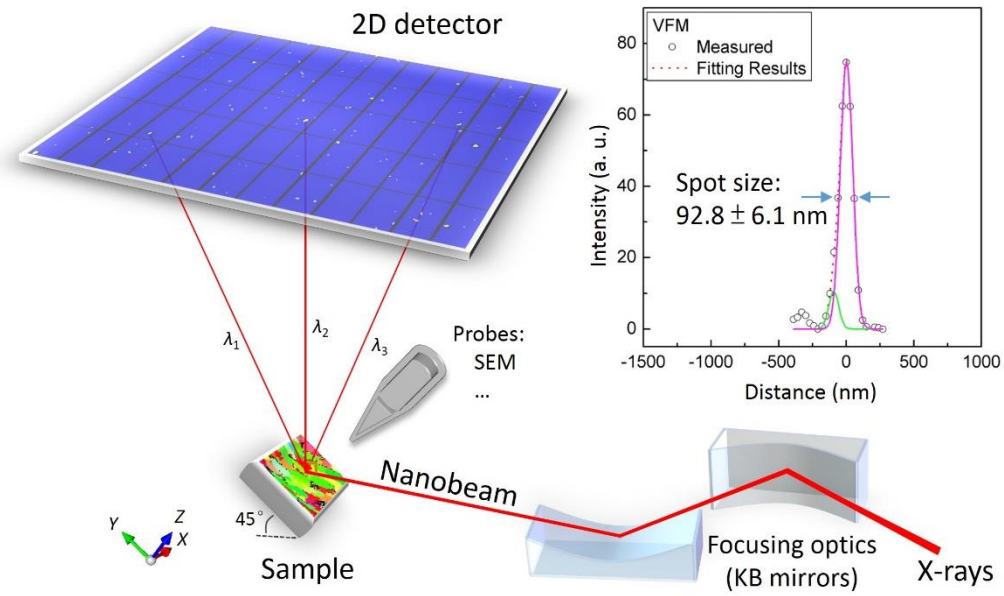

Figure S1. Schematic layout of the scanning synchrotron X-ray Laue nanodiffraction with sub-100 nm spatial resolution, Related to Figures 2-4. The polychromatic X-rays spot was focused to tens of nanometer (inserted diagram) by focusing K-B mirror optics. The sample was fixed on a holder from which high–resolution diffraction patterns were collected by a PILATUS 6M detector.

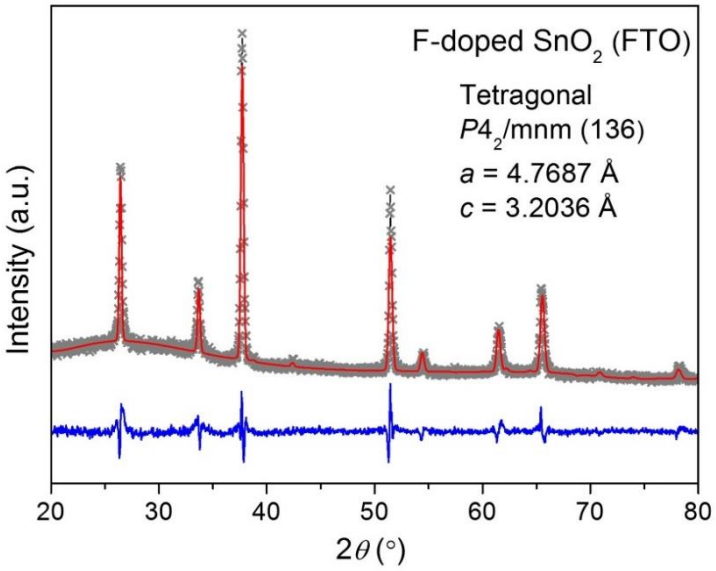

Figure S2. Rietveld refinement of the experimental XRD data of the FTO conductive glass slice at ambient conditions, Related to Figure 1 and Table 1. The refinement was performed using the *General Structure and Analysis System II* (*GSAS-II*) (Toby and Von Dreele, 2013). The blue line denotes the difference between the experiment (grey X) and refinement (red).

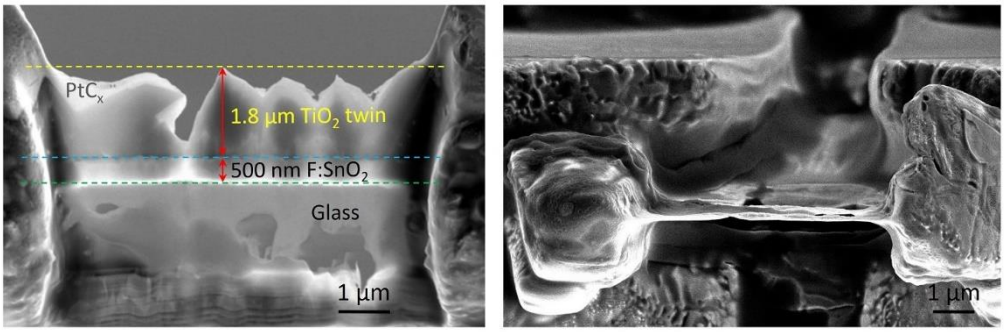

Figure S3. SEM images of the FIB-prepared TEM specimen of the rutile TiO_2 twin film, Related to Figure 1.

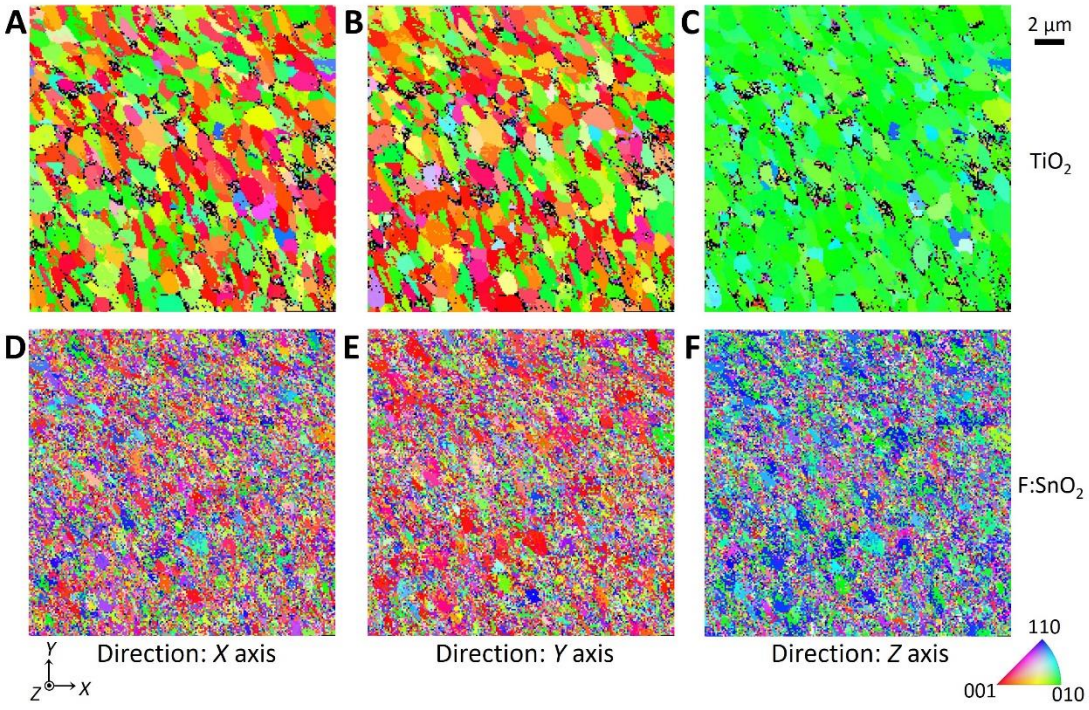

Figure S4. Crystal orientation maps of TiO_2 and F:SnO_2 along different directions in the sample coordinate system, Related to Figures 2 and 3.

(A-C) Crystal orientation maps of the TiO_2 nanotwin film.

(D-F) Crystal orientation maps of the F:SnO_2 grains substrate. The black dots represent the patterns failed to be indexed as rutile structure.

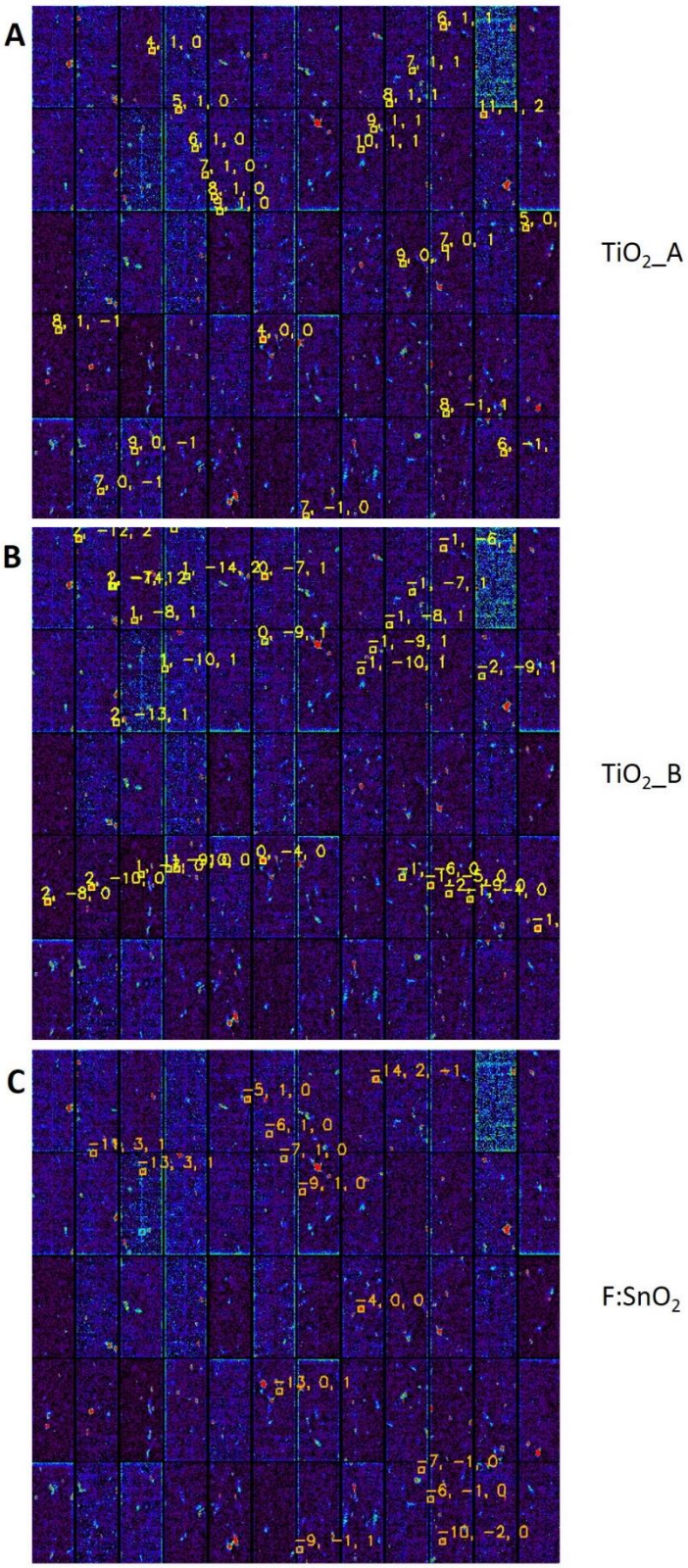

Figure S5. XND image of No. 1998 indexed to tetragonal TiO_2 (A & B) and SnO_2 (C) structure (*a* = 4.7687 Å, *c* = 3.2036 Å), respectively, Related to Figure 3. Please find the indexed results in the Supplemental Data.

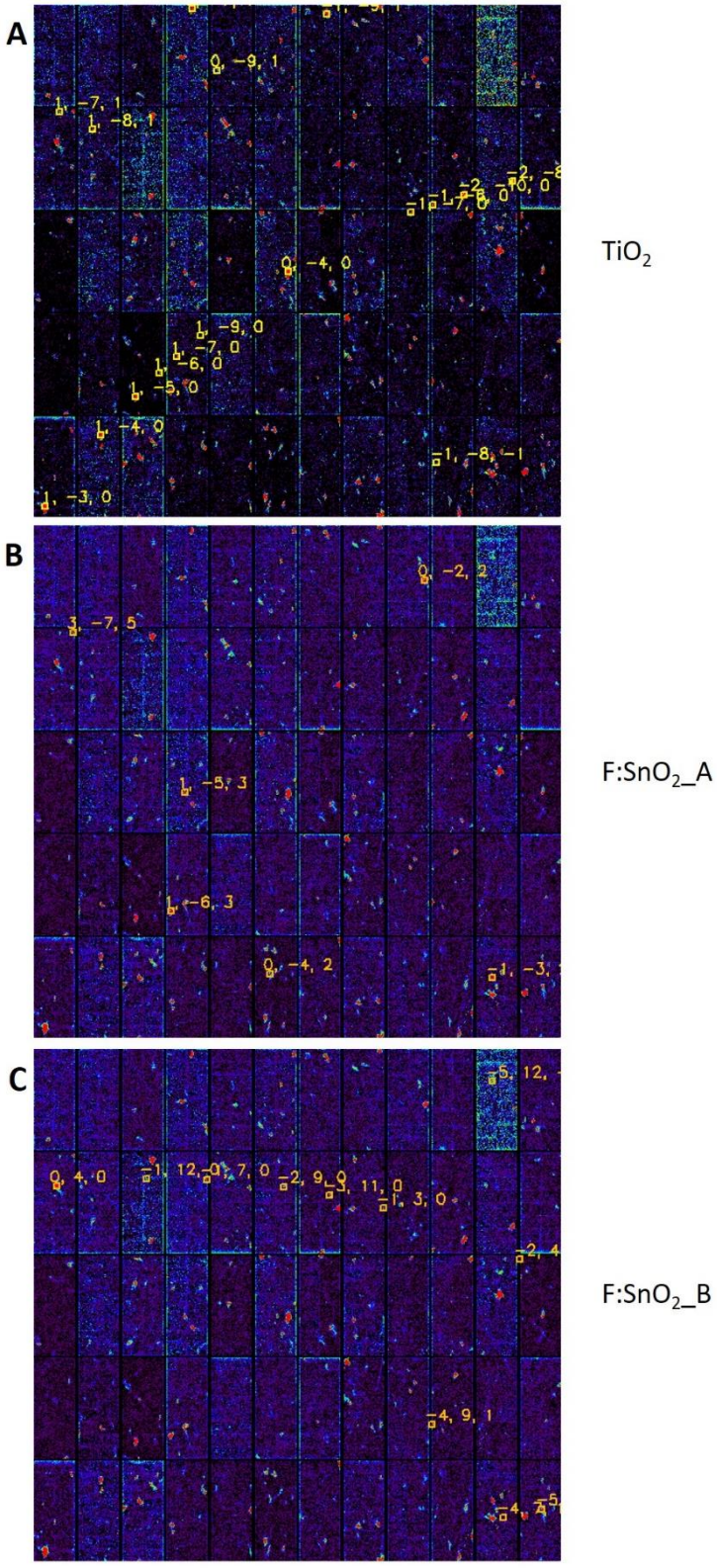

Figure S6. XND image of No. 14993 indexed to tetragonal TiO_2 (A) and SnO_2 (B & C) structure (*a* = 4.7687 Å, *c* = 3.2036 Å), respectively, Related to Figure 3.

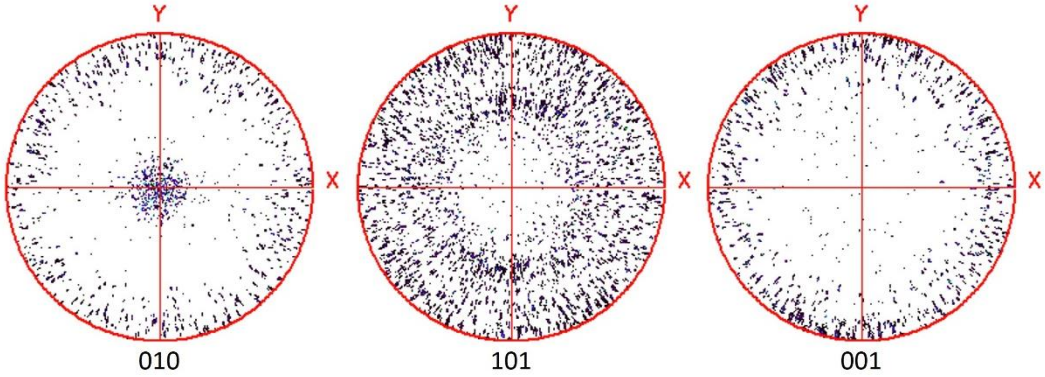

Figure S7. Pole figures of TiO_2 for all indexed XND images, Related to Figure 3.

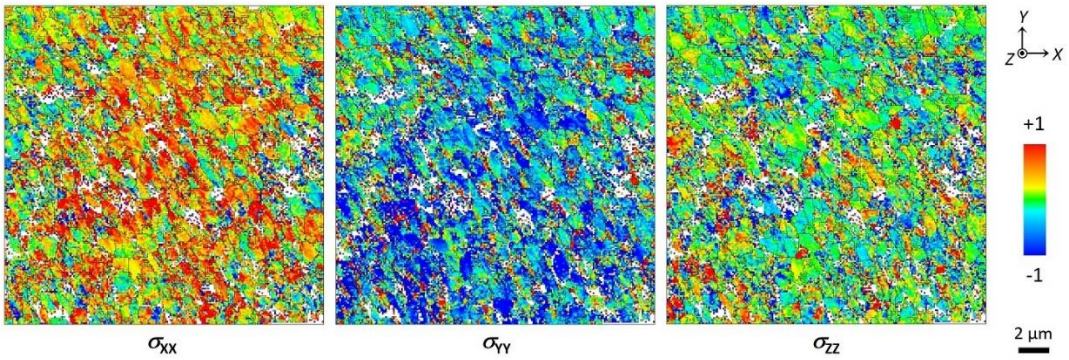

Figure S8. Spatial distribution of the normalized deviatoric stresses (overlapped with grain boundaries) in the rutile nanotwin film, Related to Figure 4.

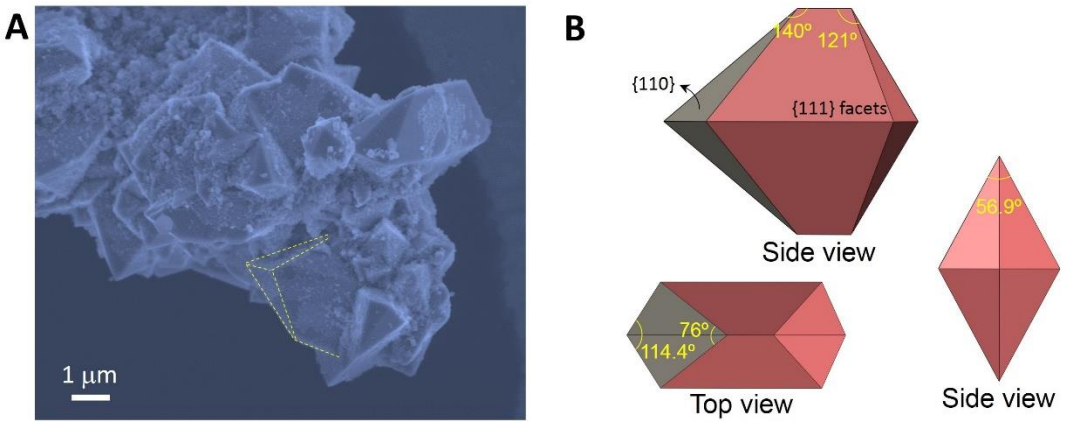

Figure S9. SEM image (A) and shape model (B) of the precipitated twinned particles in the reaction solution, Related to Figure 1 and Table 1.

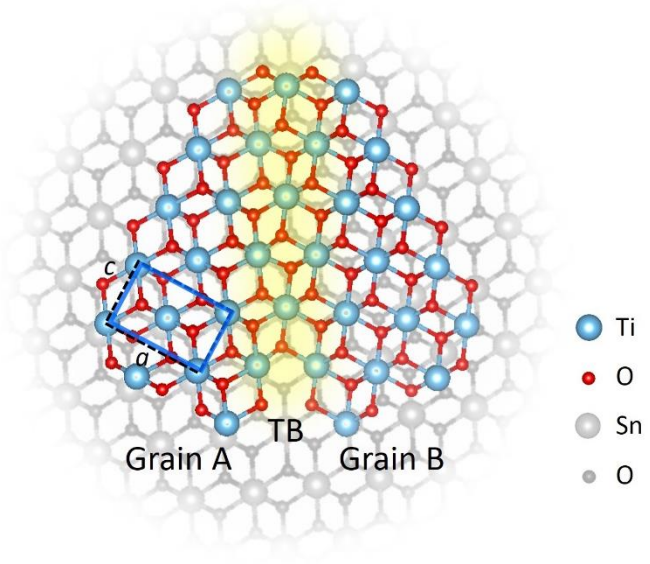

Figure S10. Scheme of the rutile TiO_2 {301} twin on the SnO_2(010) viewed along the [010] direction, Related to Figure 2 and Table 1.

Data S1. Indexed reports of the XND image No. TiO2_scan2_0001998 (tif) from XMAS, Related to Figure 3.

1. Indexed results of TiO_2_A grain

number of grains found: 1

grain no: 0 grainlist file index: 0

number of indexed reflections: 22

x(exp)	y(exp)	h	k	l	Ener(keV)	2theta(deg)
1106.695	1602.503	4	0	0	8.16582	82.75478
329.5151	2332.707	7	0	-1	16.74797	70.58026
703.5555	501.1892	5	1	0	8.79855	102.8949
574.8782	216.6063	4	1	0	6.89485	107.5996
1982.293	1165.486	7	0	1	13.56202	91.02973
2369.085	1066.217	5	0	1	9.75535	92.80698
1973.84	100.3204	6	1	1	10.35671	109.7635
1986.335	1959.834	8	-1	1	17.86347	76.66513
2261.803	2148.651	6	-1	1	14.1077	73.80907
1313.163	2453.517	7	-1	0	17.10203	67.82719
127.3696	1559.122	8	1	-1	16.58127	83.85445
1715.04	469.8182	8	1	1	14.08803	103.7079
493.0877	2141.897	9	0	-1	20.60028	73.49051
830.6199	813.3861	7	1	0	12.70187	97.39285
1777.531	1241.373	9	0	1	17.48984	89.60318
780.1652	684.0765	6	1	0	10.73812	99.70841
900.0615	990.7714	9	1	0	16.68744	94.15342
2166.246	525.0349	11	1	2	19.86192	102.4333
1575.416	690.8137	10	1	1	17.94053	99.79426
1636.77	593.6983	9	1	1	16.00582	101.5357
1821.293	311.0002	7	1	1	12.20069	106.3962
874.009	919.6783	8	1	0	14.70234	95.45995

dev1, dev2, pixdev= 0.0338600 0.0377700 0.0253900

matrix X Y Z -> h k l

0.02232 -0.02842 0.45798

0.17356 0.42498 0.01791

-0.27359 0.11088 0.02022

matrix h k l -> X Y Z

0.10577 0.82237 -3.12475

-0.13467 2.01364 1.26641

2.17001 0.08488 0.23089

Number of missing reflections: 35

Rfactor: 0.82745999

Rotangle(deg): 88.79728

Rodrigues vector: 0.16442 0.94101 0.21531 88.79728
Quaternion: 0.71449 0.11747 0.67234 0.15384
Euler angles: 79.66722 42.75689 82.67116
orsnr, orsirxy, orsirxz, orsiryz: 53.32627 67.78503 -51.50586 25.23834
Rotation matrix, unit cell to sample:
0.04859 0.37780 -0.92461
-0.06187 0.92507 0.37473
0.99690 0.03899 0.06832
Rotation matrix, sample to unit cell:
0.04859 -0.06187 0.99690
0.37780 0.92507 0.03899
-0.92461 0.37473 0.06832
Sum of integrated intensities: 8933603.00000
Average integrated intensity per peak: 446680.15625
scale: 0.00598000
depth: -0.175070
Unindexed reflections: 0
Xstage position: 43514.0
Ystage position: 11800.0
X map position: -22021
Y map position: 1
Izero: 10597.000
Channel A: 0.00000000
Channel B: 0.00000000
Channel C: 0.00000000
Channel D: 0.00000000
Channel E: 0.00000000
Exposure: 0.607000
Average intensity of the image: 92.838362
Average background of the image: 82.873988

2. Indexed results of TiO_2_B grain

number of grains found: 1

grain no: 0 grainlist file index: 0

number of indexed reflections: 27

x(exp)	y(exp)	h	k	l	Ener(keV)	2theta(deg)
1106.695	1602.503	0	-4	0	8.16582	82.75478
2424.365	1929.563	-1	-3	0	6.8009	77.72577
284.0622	1732.038	2	-10	0	21.24706	80.73582
1909.466	1721.401	-1	-5	0	10.61332	80.82959
73.95251	1803.11	2	-8	0	17.36535	79.703
2102.05	1787.395	-1	-4	0	8.67309	79.80879
1116.278	238.4037	0	-7	1	11.97984	107.735
1973.84	100.3204	-1	-6	1	10.35671	109.7635
222.8259	58.89168	2	-12	2	20.74039	109.5519
1715.04	469.8182	-1	-8	1	14.08803	103.7079
494.1708	450.5739	1	-8	1	14.10315	103.5517
522.5287	1669.975	1	-7	0	14.5915	81.67837
1776.94	1685.652	-1	-6	0	12.58823	81.39429
1115.37	549.5213	0	-9	1	15.8245	102.3036
1821.293	311.0002	-1	-7	1	12.20069	106.3962
389.9437	286.9494	2	-14	2	24.43778	106.1684
2000.909	1764.839	-2	-9	0	19.33087	80.1202
743.8867	237.2892	1	-14	2	24.05987	107.4615
695.955	1642.875	1	-10	0	20.65261	82.09056
654.776	1644.174	1	-9	0	18.61041	82.08256
2158.033	714.6269	-2	-9	1	16.57559	99.12955
1577.617	692.2443	-1	-10	1	17.944	99.76793
637.6443	679.6884	1	-10	1	17.95503	99.68447
383.8218	284.9153	1	-7	1	12.21694	106.1928
1634.819	590.6048	-1	-9	1	15.99944	101.5917
406.287	942.7387	2	-13	1	24.2765	94.81672
680.4789	8.1313	1	-12	2	20.34551	111.1356

dev1, dev2, pixdev= 0.0726400 0.0619900 0.0485500

matrix X Y Z -> h k l

0.45854 0.01915 -0.02052

-0.02169 0.02868 -0.45799

-0.01147 0.29507 0.01902

matrix h k l -> X Y Z

2.17269 -0.10279 -0.13099

0.09072 0.13590 3.36999

-0.09723 -2.17007 0.21725

Number of missing reflections: 72

Rfactor: 0.62246001
Rotangle(deg): 86.42025
Rodrigues vector: 0.93847 -0.00278 -0.04184 86.42094
Quaternion: 0.72884 0.68400 -0.00203 -0.03049
Euler angles: 86.31144 2.21962 -2.70861
orsnr, orsirxy, orsirxz, orsiryz: 53.56714 2.39092 -0.67673 53.56610
Rotation matrix, unit cell to sample:
0.99813 -0.04722 -0.03876
0.04168 0.06243 0.99718
-0.04467 -0.99693 0.06429
Rotation matrix, sample to unit cell:
0.99813 0.04168 -0.04467
-0.04722 0.06243 -0.99693
-0.03876 0.99718 0.06429
Sum of integrated intensities: 14591121.00000
Average integrated intensity per peak: 583644.81250
scale: 10.9890
depth: -0.264670
Unindexed reflections: 0
Xstage position: 43514.0
Ystage position: 11800.0
X map position: -22021
Y map position: 1
Izero: 10597.000
Channel A: 0.00000000
Channel B: 0.00000000
Channel C: 0.00000000
Channel D: 0.00000000
Channel E: 0.00000000
Exposure: 0.607000
Average intensity of the image: 92.838362
Average background of the image: 82.873988

3. Indexed results of F:SnO_2 grain

The indexed reflections from TiO_2 were masked to reduce the interference.

number of grains found: 1

grain no: 0 grainlist file index: 0

number of indexed reflections: 13

x(exp)	y(exp)	h	k	l	Ener(keV)	2theta(deg)
1575.453	1244.985	-4	0	0	7.38595	89.50503
1968.467	2359.248	-10	-2	0	23.14313	69.89858
1034.028	235.7058	-5	1	0	8.20737	107.7363
1208.45	523.1463	-7	1	0	11.7619	102.8047
1868.458	2020.032	-7	-1	0	15.01524	75.49885
1298.06	682.6916	-9	1	0	15.3738	99.94311
1184.172	1639.877	-13	0	1	25.9119	82.06355
1138.206	403.6893	-6	1	0	9.97449	104.8938
1911.1	2159.014	-6	-1	0	13.2699	73.15503
1283.73	2400.521	-9	-1	1	21.14641	68.68884
1645.708	140.9373	-14	2	-1	22.65584	109.3669
294.0976	495.5388	-11	3	1	19.1628	102.5327
529.8547	583.9432	-13	3	1	22.57164	101.2806

dev1, dev2, pixdev= 0.0818400 0.0648700 0.0430400

matrix X Y Z -> h k l

0.03029 0.00120 -0.47590

0.28079 0.38497 0.01884

0.25813 -0.18906 0.01595

matrix h k l -> X Y Z

0.13320 1.23478 2.51518

0.00528 1.69292 -1.84212

-2.09279 0.08286 0.15544

Number of missing reflections: 99

Rfactor: 0.69611001

Rotangle(deg): 92.27490

Rodrigues vector: -0.32784 -0.93915 0.30527 92.27490

Quaternion: 0.69293 -0.22717 -0.65076 0.21153

Euler angles: -85.17680 -38.86055 83.84298

orsnr, orsirxy, orsirxz, orsiryz: 53.28348 53.89382 46.65455 -88.82387

Rotation matrix, unit cell to sample:

0.06352 0.58882 0.80576

0.00252 0.80730 -0.59014

-0.99798 0.03951 0.04980

Rotation matrix, sample to unit cell:

0.06352 0.00252 -0.99798

0.58882 0.80730 0.03951

0.80576 -0.59014 0.04980

Sum of integrated intensities: 2007949.12500

Average integrated intensity per peak: 182540.82813

scale: -0.00419000

depth: -0.187010

Unindexed reflections: 0

Xstage position: 43514.0

Ystage position: 11800.0

X map position: -22021

Y map position: 1

Izero: 10597.000

Channel A: 0.00000000

Channel B: 0.00000000

Channel C: 0.00000000

Channel D: 0.00000000

Channel E: 0.00000000

Exposure: 0.607000

Average intensity of the image: 92.838362

Average background of the image: 82.873988

Supplemental References

Chen, X., Dejoie, C., Jiang, T., Ku, C.-S., and Tamura, N. (2016). Quantitative microstructural imaging by scanning Laue x-ray micro- and nanodiffraction. *MRS Bull.* 41, 445-453.

Li, Y., Wan, L., and Chen, K. (2015). A look-up table based approach to characterize crystal twinning for synchrotron X-ray Laue microdiffraction scans. *J. Appl. Crystallogr.* 48, 747-757.

Lu, Y., Chiang, C.-Y., and Huang, E. (2020). Vertically nanotwinned TiO_2 photoanodes with enhanced charge transport for efficient solar water splitting. *Appl. Mater. Today* 20, 100707.

Toby, B. H., and Von Dreele, R. B. (2013). GSAS-II: the genesis of a modern open-source all purpose crystallography software package. *J. Appl. Crystallogr.* 46, 544-549.